NANO LETTERS

2005
Vol. 5, No. 10
2097−2103

Superhydrophobicity and Superhydrophilicity of Regular Nanopatterns

Elena Martines,[†] Kris Seunarine,[‡] Hywel Morgan,[§] Nikolaj Gadegaard,[‡] Chris D. W. Wilkinson,[‡] and Mathis O. Riehle*,[†]

Centre for Cell Engineering, IBLS, University of Glasgow, Glasgow, G12 8QQ, U.K., Department of Electronics and Electrical Engineering, University of Glasgow, Glasgow, G12 8QQ, U.K., and School of Electronics and Computer Science, University of Southampton, S017 1BJ, U.K.

Received July 25, 2005

ABSTRACT

The hydrophilicity, hydrophobicity, and sliding behavior of water droplets on nanoasperities of controlled dimensions were investigated experimentally. We show that the "hemi-wicking" theory for hydrophilic SiO_2 samples successfully predicts the experimental advancing angles and that the same patterns, after silanization, become superhydrophobic in agreement with the Cassie–Baxter and Wenzel theories. Our model topographies have the same dimensional scale of some naturally occurring structures that exhibit similar wetting properties. Our results confirm that a forest of hydrophilic/hydrophobic slender pillars is the most effective superwettable/water-repellent configuration. It is shown that the shape and curvature of the edges of the asperities play an important role in determining the advancing angles.

Introduction. The wettability of solid surfaces is a subject that has raised great interest in the past few decades. The surface energy of a sample will determine if a given liquid drop will roll up or spread when deposited on it. Roughening the surface enhances its repellent or wetting properties,[1] resulting in "superhydrophobic" or "superhydrophilic" textures (this nomenclature applies if the liquid considered is water, as is the case in this work).

Many authors have contributed to the fabrication and understanding of superhydrophobic surfaces.[2−14] Öner and McCarthy[10] describe a superhydrophobic surface as one where the advancing angle, θ_{adv}, is very high (generally $>150°$), and the receding angle, θ_{rec}, is such that the drop exhibits low hysteresis $\Delta\theta$ ($\Delta\theta = \theta_{adv} - \theta_{rec}$). Water drops form beads and roll off this kind of surface, cleaning it in the process. This phenomenon has been termed the "Lotus effect" because it is very pronounced on the leaves of the lotus plant (*Nelumbo nucifera*).[14,15] These leaves exhibit a double-structured roughness, where submicrometric wax crystals cover a larger micrometric structure; even though double-scale roughness has been proven to enhance water repellency,[16] it has been suggested that the small scale roughness plays an important role.[12] The wings of some insects (e.g., *Pflatoda claripennis* and in the family Rhinotermitidae) are also covered with nanometric structures that are thought to ensure water repellency as well as other properties;[17] unlike the irregular topography of wax crystals, these surfaces are covered with ordered arrays of rounded protrusions.

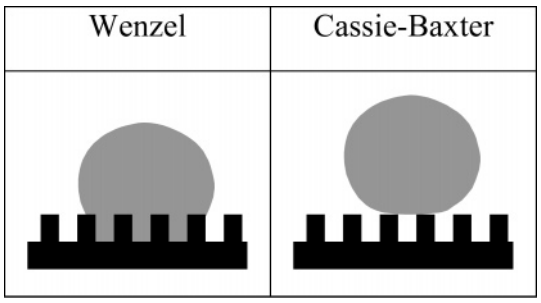

Figure 1. Schematic of roughness-filling by water according to the Wenzel and Cassie−Baxter models.

The effect of surface roughness on hydrophobicity has been explained by two different theories. According to the model developed by Wenzel, it is assumed that the space between the protrusions on the surface is filled by the liquid[3] (Figure 1); this model predicts that both hydrophobicity and hydrophilicity are reinforced by the roughness,

* Corresponding author. E-mail: m.riehle@bio.gla.ac.uk; tel: 0044-141-3302931; fax: 0044-141-3303730.
[†] Centre for Cell Engineering.
[‡] Department of Electronics and Electrical Engineering.
[§] University of Southampton.

10.1021/nl051435t CCC: $30.25
Published on Web 10/12/2005

according to the following relation

$$\cos \theta_W = r \cos \theta_Y \quad (1)$$

where θ_W is the apparent contact angle on a rough surface, θ_Y is the ideal contact angle (Young's angle) of water on a smooth surface of identical chemistry, and r is the roughness factor, which is defined as the ratio of actual surface area over the projected area.

The approach developed by Cassie and Baxter, however, assumes that air is trapped by the asperities[2] so that the drop sits on a composite surface made of air and solid (Figure 1); the relation between the apparent contact angle θ_{CB} and the ideal angle θ_Y is in this case described as

$$\cos \theta_{CB} = r_f f \cos \theta_Y + f - 1 \quad (2)$$

where r_f is the roughness factor of the wetted area, and f is the area fraction of the projected wet area. The product $r_f f$ is often called the solid fraction ϕ_S.

Both Wenzel and Cassie−Baxter relations were originally formulated for static drops at equilibrium; yet because it was shown that low-rate advancing angles and static angles are essentially identical,[18] eqs 1 and 2 can be applied to advancing angles. Fewer attempts have been made to model the receding angles.[11,19] It has been shown[4] that a droplet can be in either a Cassie−Baxter or a Wenzel state on a rough hydrophobic surface depending on how it is formed. Because the advancing angles predicted by both the Cassie−Baxter and Wenzel theories can be very close to the experimental values, the receding angles can be used as a qualitative indication of the state of the drop: if θ_{rec} is high (i.e., the hysteresis is low), then the drop will be in a Cassie−Baxter ("slippy") mode; if θ_{rec} is low, then the drop will be in a Wenzel ("sticky") state. Therefore, obtaining a stable Cassie−Baxter drop is the ultimate goal for achieving superhydrophobicity by tailoring surface topography. The adhesive behavior of water on rough surfaces can also be assessed by sliding-angle measurements.[5,6,9] The sliding angle is defined as the critical angle where a water droplet begins to slide down an inclined plate: a high sliding angle indicates a sticky Wenzel state, whereas a low sliding angle suggests a Cassie−Baxter regime (i.e., the drop will easily roll off a slightly tilted substrate).[4]

Much less work has been dedicated to the study of superhydrophilic (or more generally, superwetting) surfaces.[1,20,21] Assuming that no air is trapped in the roughness of the hydrophilic surface (for the opposite case, see Abdelsalam et al.[22]), the Wenzel model still applies, along with the hemi-wicking or "composite-drop" model,[23] where the drop is assumed to be sitting on a composite surface made of solid and water.

All of the above-mentioned theories for both hydrophobic and hydrophilic rough surfaces have been tested by preparing surfaces structured on the micrometer scale;[5−7,9,10,14,16,20] only a few studies have been done recently on nanotopographies,[8,22,24,25] mainly because of the difficulty of fabrication.

In the present study, we have fabricated ordered arrays of nanopits and nanopillars and investigated their dynamic wettability before and after chemical hydrophobization. Our model structures resemble the natural submicrometric features that ensure the water repellency of biological surfaces such as the lotus leaf and some insect wings.

Because of the accurate geometrical characterization of our nanopatterns, the validity of the analytical models currently available for predicting the wettability of rough surfaces can be verified, for both the hydrophilic and the hydrophobic case. To the best of our knowledge, this is the most extensive quantitative study of the wetting properties of small-scale topography reported so far.

Experimental Details. *(A) Fabrication.* Nanopatterns with increasing solid fraction (two samples with pits and four with pillars) were fabricated in silicon wafers (4 in., ⟨100⟩, p-doped, 525 ± 50 μm thick) across an area of 1 × 1 cm^2. (1) Nanopillars. A 2-nm titanium layer was evaporated on the silicon (Plassys evaporator), and the samples were spin-coated immediately with a 60% NEB31A3−40% EC solvent (Sumitomo Chemical Co Ltd) at 3 krpm for 60 s (150-nm-thick coating). After a preexposure bake at 90 °C for 2 min, the wafers were exposed in the e-beam writer (Leica Microsystems EBPG 5) with the desired pattern. After a postexposure bake at 85 °C for 2 min, we developed the samples in Microposit MF CD-26 for 20 s and rinsed them with reverse osmosis (RO) water; the titanium was etched (1 part HF: 26 parts RO water) for approximately 2−3 s, and the samples were rinsed in RO water. The silicon was then dry-etched using STS-ICP (Surface Technology Systems-Inductively Coupled Plasma) with C_4F_8 and SF_6 (unswitched gases) at an etch rate of 100 nm/min, and finally piranha-cleaned for 5 min. (2) Nanopits. The silicon wafers were spin-coated with 40% ZEP520A at 5 krpm (100-nm-thick coating) and baked at 180 °C for 1 h. The samples were then exposed in the e-beam writer, developed in *o*-xylene for 60 s, and dry-etched as for the pillars. Finally, the surfaces were piranha-cleaned for 5 min.

(B) Surface Modification. Prior to the measurements of contact angles on the hydrophilic nanopatterns, we cleaned all of the samples with an O_2 plasma for 15 min (BP80 RIE, flow rate 20 sccm, pressure 30 mT, RF power 100 W); the contact angles on these surfaces were measured within 24 h.

Subsequently, the same patterns were coated with octadecyltricholorosilane (OTS) by modifying the procedure of Rosloznik et al.:[26] all of the samples were sonicated for 10 s in 1:1 water−ethanol and 10 s in IPA, then rinsed in chloroform and blow-dried. After a 15 min O_2 cleaning, we sonicated them for 10 s in chloroform and 10 s in IPA, rinsed them in 1:1 water−ethanol, rinsed them in RO water, and blow-dried them. The clean samples were then placed in a ceramic slide holder, which was gently tilted on the side at 90° so that the patterns were facing down. This technique ensured that if any OTS clusters formed in the solution, then they had less of a chance of being deposited on the patterned surfaces. The tilted holder was placed in a glass beaker filled with a 0.001% solution of OTS (Sigma) in heptane (Sigma).

After 3.5 h, we sonicated the holder three times for 1 min in copious amounts of heptane, then rinsed it in IPA, 1:1 water−ethanol, and RO water and finally blow-dried it.

(C) Sample Characterization. (1) Scanning Electron Microscopy. The surfaces were imaged with a Hitachi S4700 prior to and following hydrophobization. After contact angle measurements, we cleaved them and their SEM profiles were used to measure the dimensions of the asperities with ImageJ.[27] (2) Dynamic Contact Angle Measurements. Images of the advancing and receding contact angles of filtered Milli-Q water were captured at a rate of 2 images/s with a long-distance objective connected to a CCD camera and analyzed with the FTÅ200 software (First Ten Ångstroms, v2.0). Water drops were deposited and taken up through a 30-gauge flat-tipped needle, at a rate of 0.25 μL/s; the maximum volume of the drops was 5 μL on hydrophobic substrates and 4 μL on hydrophilic ones. The values reported are averages of at least five measurements made on different areas of the sample. All of the measurements were performed at room temperature on a vibration-free platform. (3) Sliding-Angle Measurements. For sliding-angle measurements on the hydrophobic samples, water drops of weight ranging from 5 to 40 mg were deposited gently on a horizontal plate fixed on a goniometer by means of a calibrated micropipet. The goniometer was rotated slowly until the drops started to slide. The sliding angle was determined on at least four different locations/sample.

Theoretical Models. *(A) Hydrophobic Surfaces*. For vertical structures with a flat top, assuming that the water does not invade the roughness, then $r_f = 1$ and $\phi_S = f$. In this work, ϕ_S always refers to the solid fraction of cylindrical pillars $\phi_S = \pi d^2/4l^2$, where d is the base diameter of the cylinders, and l is their center-to-center pitch. We applied the Cassie−Baxter and Wenzel formulas to different geometries. (1) The Cassie−Baxter relation was calculated for two cases:

cylindrical asperities:

$$\cos\theta_{CB-c} = -1 + \phi_S(\cos\theta_Y + 1) \quad (3)$$

hemispherical-top pillars:[7]

$$\cos\theta_{CB-h} = -1 + \phi_B(\cos\theta_Y + 1)^2 \quad (4)$$

where ϕ_B is the ratio of the area of the asperity bases over the total area. In our case, $\phi_B = \phi_S$. (2) Wenzel's relation was calculated for two cases:

cylindrical asperities:

$$\cos\theta_{W-c} = r\cos\theta_Y \quad (5)$$

hemispherical-top pillars:

$$\cos\theta_{W-h} = \left[1 + 4\phi_S\left(\frac{h}{d} - 0.25\right)\right]\cos\theta_Y \quad (6)$$

We also calculated the receding angle of composite drops by assuming that a receding drop leaves a film of water behind.[19] In this way, Patankar[11] derived eq 7 to predict the receding angles on asperities with a flat top ($r_f = 1$). We applied eq 7 to cylindrical pillars

$$\cos\theta_{rec-c} = 2\phi_S - 1 \quad (7)$$

In the case of hemispherical asperities, eq 7 becomes

$$\cos\theta_{rec-h} = \phi_S(2 + 2\cos\theta_Y + \sin^2\theta_Y) - 1 \quad (8)$$

(B) Hydrophilic Surfaces. We applied the composite-drop (or hemi-wicking) and the Wenzel formulas to different geometries. (1) The composite-drop relation was calculated for two cases:

cylindrical asperities:[23]

$$\cos\theta_{comp-c} = 1 + \phi_S(\cos\theta_Y - 1) \quad (9)$$

hemispherical-top pillars:

$$\cos\theta_{comp-h} = \phi_S(2\cos\theta_Y + 3\cos^2\theta_Y - 1) + 1 \quad (10)$$

(2) Wenzel's relation was applied to the case of cylindrical pillars, as in eq 5.

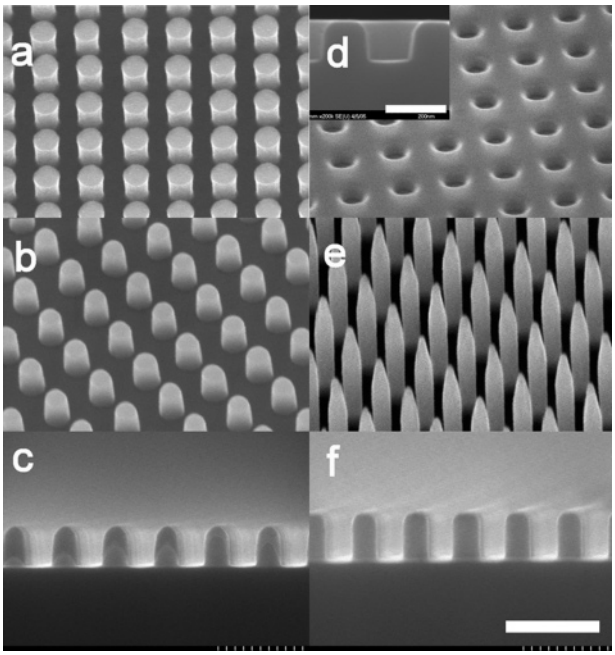

Figure 2. SEM images of (a) P22 before hydrophobization; (b) P22 after hydrophobization; (c) profile of P22; (d) sample H83 after hydrophobization, the insertion shows its profile; (e) P12 after hydrophobization; (f) profile of P21. The profiles were imaged with a 90° tilt, the other images were taken at 45°, scale bar = 500 nm (a−f) and 200 nm (inset in d), respectively.

Table 1. Dimensions of the Nanopatterns[a]

	H90	H83	P22	P21	P13	P12
d (nm)	105	138	157	156	124	117
h (nm)	116	141	239	286	268	792
l (nm)	300	300	300	300	300	300

[a] All dimensions were measured with ImageJ (±5 nm). In case of hollow asperities (H), h indicates the depth. In case of pillars (P), h indicates the maximum distance from the base to the top.

Table 2. Experimental Angles of Water on Hydrophobic (5 μL Drop) and Hydrophilic (4 μL Drop) Nanopatterns[a]

		flat	H90	H83	P22	P21	P13	P12
hydrophobic	θ_{adv}(deg)	114 ± 1	125 ± 2	129 ± 3	155 ± 2	159 ± 2	161 ± 2	164 ± 2
	θ_{rec}(deg)	100 ± 3	92 ± 2	89 ± 2	0	140 ± 2	150 ± 2	163 ± 2
	model		W-c	W-c	W-h	CB-h	CB-h	CB-h
hydrophilic	θ_{adv}(deg)	35 ± 3	36 ± 3	35 ± 3	12 ± 3	19 ± 3	11 ± 3	0
	θ_{rec}(deg)	0	0	0	0	0	0	0
	model		comp-c	comp-c	comp-c	comp-c	comp-c	comp-h

[a] Advancing and receding angles are shown, along with the best theoretical agreement (model): (W) Wenzel, (CB) Cassie−Baxter and (comp) composite-drop, with (-c) cylindrical and (-h) hemispherical top.

Results and Discussion. *(A) Sample Characteristics.* SEM images of the patterns immediately after fabrication showed perfectly cylindrical nanopillars and nanopits, except for sample P12, where the tall pillars had a cusped top. The edges of the pillars were rounded after hydrophobization because of sonication. This is summarized in Figure 2a−b. In particular, sample P22 has pillars with a hemispherical top (Figure 2c), and the others look like cylinders with smooth edges (Figure 2f), except P12 whose shape was unchanged after coating (Figure 2e). The pitted samples (Figure 2d) had a cylindrical profile. The different patterns were named after their solid fraction percentage (H designates a hollow pattern, i.e., pits, P a protruding pattern, i.e., pillars; P22 indicates a pillared sample where 22% of the apparent area is wet by the drop, assuming a cylindrical top). Table 1 shows the dimensions of the patterns (base diameter *d*, height *h*, center-to-center pitch *l*). The contact angle measured on the OTS-coated flat silicon was $114 \pm 1°$, which indicates that a monolayer was formed (a contact angle for total coverage was reported to be 115°).[26]

(B) Hydrophilic Patterns: Experiments and Predictions. The experimental advancing and receding angles (θ_{adv} and θ_{rec}) on hydrophilic silicon are shown in Table 2. The experimental advancing angles along with the theoretical predictions are plotted in Figure 3. Because all of the structures (except P12) were perfectly cylindrical, the Wenzel and composite-drop curves were plotted for this geometry; the composite-drop curve for hemispherical-top pillars is also shown for comparison with the experimental advancing angle on P12. Young's angle for these substrates was taken as the angle measured on the flat control ($\theta_Y = 35 \pm 1°$). The receding drops on these substrates were pinned ($\theta_{rec} = 0°$), as predicted by Quere.[23]

Figure 3 shows that the composite-drop formula for cylindrical asperities is in excellent agreement with the experimental values, except for sample P12 where $\theta_{adv} = 0°$. It should be noted that both the Wenzel formula for cylinders and the composite-drop formula for hemispherical tops (eq 10) always predict an apparent angle of 0°, which is theoretically unattainable because $\cos\theta > 1$. Therefore, the topography-induced superhydrophilicity of sample P12 was due to the high aspect ratio, *h*/*d*, of the protrusions, which acted as a reservoir for the fast spreading of the liquid front,[23] a spreading much faster than that on the flat surface.[21] Because the composite-drop relation does not depend on the aspect ratio of the features, this formula predicts that hemispherical-top pillars will always be superhydrophilic.

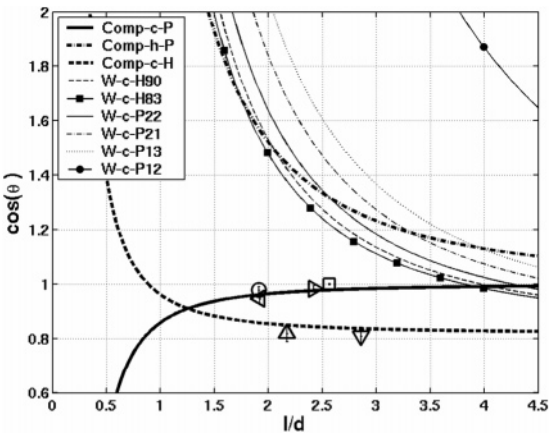

Figure 3. Plot of the apparent advancing angles of a 4-μL drop of water on hydrophilic patterns as a function of structure geometry. composite drop (comp-) and Wenzel (W-) curves for cylindrical (-c-) and hemispherical (-h-) asperities are shown. The Wenzel curves were plotted for cylindrical asperities only. The composite drop curves for pillars, P, and pits, H, are different because of a different dependence on *l*/*d*. Individual points indicate experimental data: (△) H90; (▽) H83; (○) P22; (left-facing triangle) P21; (right-facing triangle) P13; (□) P12.

In this context, it would be interesting to investigate the effect of height variation on the reservoir-effect of such structures.

(C) Hydrophobic Patterns: Experiments and Predictions. The experimental advancing and receding angles (θ_{adv} and θ_{rec}) on hydrophobic silicon are shown in Table 2. Young's angle for these substrates was taken as the advancing angle measured on the flat control ($\theta_Y = 114° \pm 1$). The experimental advancing angles along with the theoretical predictions are plotted in Figure 4.

Because the end-geometries of the hydrophobized pillars were somewhat between cylindrical and hemispherical, the Cassie−Baxter and Wenzel curves were plotted for both geometries (eqs 3 and 5 in Figure 4a, and eqs 4 and 6 in Figure 4b), whereas the pits were always modeled as perfect cylinders (eqs 3 and 5). The sliding angles in Figure 5 were used as a means to test the predictions derived from Figure 4 concerning the "state" of the drops (i.e., Cassie−Baxter or Wenzel).

In the following paragraphs, we discuss our results within the framework of Patankar's criterion for designing superhydrophobic surfaces.[11] Briefly, this method consists of obtaining a stable Cassie−Baxter drop by fabricating structures, which, given the highest possible aspect ratio, *h*/*d*, have a dimensionless spacing, *l*/*d*, such that $\cos\theta_{CB} > \cos\theta_W$, or

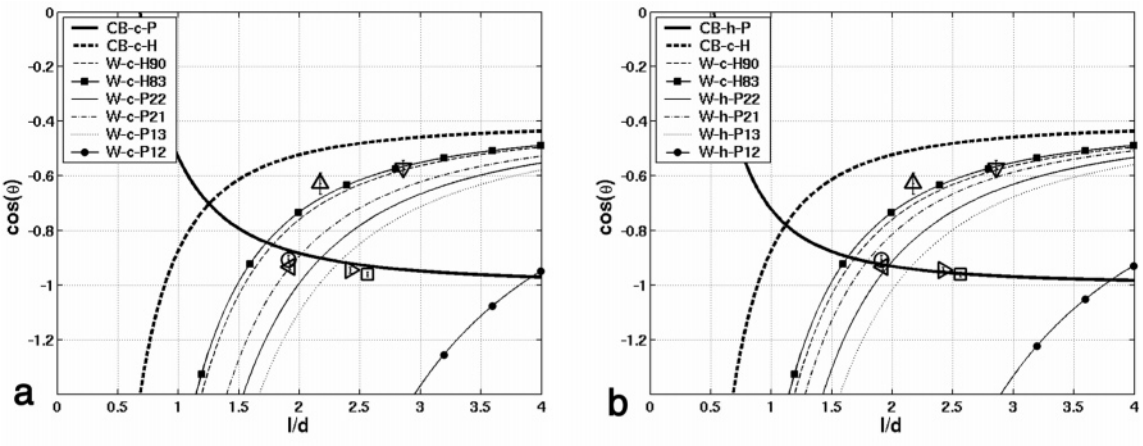

Figure 4. Plot of the apparent advancing angles of a 5-μL drop of water on hydrophobic patterns as a function of structure geometry. (a) Cassie−Baxter (CB-) and Wenzel (W-) curves for cylindrical asperities (-c-). (b) Cassie−Baxter (CB-) and Wenzel (W-) curves for cylindrical asperities (-c-) and cylinders with hemispherical tops (-h-). The CB and W curves for pits H90 and H83 are the same (W-c-H) in a and b, whereas the CB and W curves for pillars are different: in a the pillars (P) are modeled as cylinders; in b they are modeled as cylinders with hemispherical tops. Note that the dependence of the CB curve on l/d for pillars and pits (CB-c-H and CB-c-P) is different. Individual points indicate experimental data: (△) H90; (▽) H83; (○) P22; (left-facing triangle) P21; (right-facing triangle) P13; (□) P12.

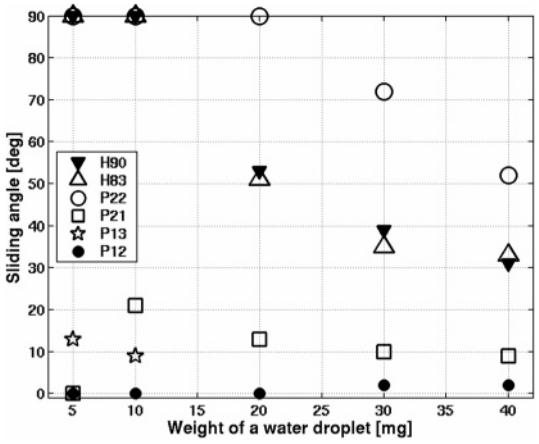

Figure 5. Sliding angles of water droplet on hydrophobic patterns as a function of drop weight. The points at 90° indicate pinned drops.

a value of $|\cos\theta_W - \cos\theta_{CB}|$ as high as possible; the first condition ensures that a Cassie−Baxter drop will have lower energy than a Wenzel drop for the given geometry; the second condition means that even if $\cos\theta_{CB} < \cos\theta_W$, then the energy barrier between the two states should be as high as possible to avoid transitions from a metastable Cassie−Baxter drop to a lower-energy Wenzel state.

The experimental values of the advancing angles on the pitted samples (H90 and H83) were in agreement with their respective Wenzel curves for cylindrical pits (same W-c-H in both Figure 4a−b). This was supported by sliding-angle measurements, where 5−10 mg drops were completely pinned (Figure 5). This result goes against theoretical expectations because the Cassie−Baxter curve for pits (CB-c-H) is always at a lower energy than the Wenzel one (W-c-H), that is, $\cos\theta_{CB-c-H} > \cos\theta_{W-c-H}$. However, the Cassie−Baxter regime for pits is stabilized only for $l/d < 1.54$ (H90) and $l/d < 1.48$ (H83), which are the critical values at which the corresponding Wenzel angles become unattainable ($\cos\theta_W < -1$); it is therefore possible to obtain a higher energy configuration with our topography. However, this predicts the occurrence of stable Cassie drops on pitted surfaces with a high density of pits of large diameters.

The best agreement with the experimental data for pillars was found with the models using a hemispherical top (Figure 4b), even when the tops were not perfectly hemispherical (e.g., as in Figure 2f). This underlines the importance of the curvature of the edges in determining the advancing angles. From now on, we will refer to the results plotted in Figure 4b.

Samples P22 and P21 had practically the same ϕ_S values, but different roughness values, r. Their experimental advancing angles were close to the intersection between the Cassie−Baxter curve for pillars and their Wenzel curves. In this case, the receding angles should allow us to distinguish if the drops were in either a Wenzel or a Cassie−Baxter state. On receding, the water droplets were pinned on P22 ($\theta_{rec} = 0°$) because the receding angle never attained a steady state. The sliding-angle measurements showed that drops of up to 20 mg were pinned on this substrate (upper 90° values in Figure 5). This result suggests that P22 is in a Wenzel state; this could be explained by the fact that P22 is the shallowest of the four protruding patterns and it has truly hemispherical edges: both factors make the Cassie−Baxter regime more unlikely to happen because sharp edges and a high aspect ratio are important conditions to ensure air trapping.[7] Öner and McCarthy[10] showed that the receding angles depended on the three-phase contact line structure, whereas the advancing angles were unaffected by it. We suggest that the unusual pinning on sample P22 might be due to the curvature of the hemispherical tops (see Figure 2c) because the contact line could be pinned by greater solid−liquid contact and indeed a hemispherical top will have more solid−liquid contact than a flat top with the same height ($\Delta\phi_S = 4\%$ for P22). However, a receding angle of 0° was unexpected, and we have no explanation for this; between the possible reasons we cannot exclude a differential hydrophobization of the

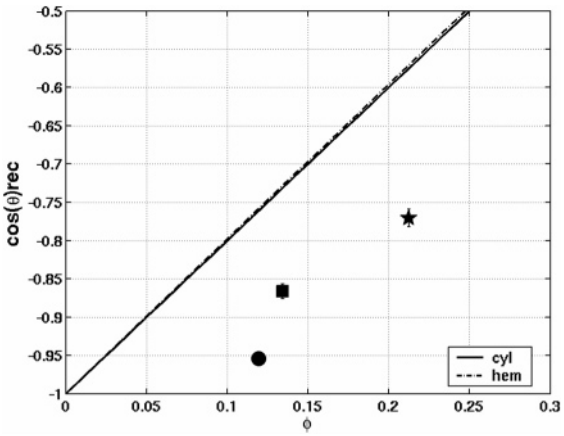

Figure 6. Receding angles of water on hydrophobic patterns as a function of the solid fraction, ϕ_S. The experimental values ((★) P21; (■) P13; (●) P12) are plotted with eq 7 (cyl) and eq 8 (hem).

bottom surface compared to the top of the asperities, which would have affected the receding angles on the Wenzel samples; still, only P22 showed this behavior.

Unlike P22, sample P21 had a high receding angle, showing that it was in a Cassie state. Its closeness to the critical point would imply that a transition to the Wenzel state would need very little energy; this hypothesis was confirmed by the tilting angle measurements, which showed a sudden jump from 0 to 21° when the drop weight was increased from 5 to 10 mg. The increased weight forced the water inside the texture, and the 10-mg drop transitioned to the Wenzel state.

For sample P13, a Wenzel state would have a lower energy, but the energy barrier to overcome is bigger than that in P21. In this case, an increase in drop weight from 5 to 10 mg caused a decrease in sliding angle, confirming the Cassie−Baxter state of the 5-μL droplet.

Sample P12 had the best water-repellent configuration not only because the Cassie−Baxter state was at lower energy than the Wenzel state and the energy barrier between the two was very high but also because the Wenzel angle corresponding to this geometry is unattainable ($\cos\theta_W < -1$). Tilting angles on P12 were $0 \pm 2°$ throughout the whole range of drop weights, making it impossible to deposit a drop smaller than 30 μL. This finding is coherent with Patankar's prediction that a forest of nanopillars would be the most effective water-repellent structure,[12] confirming that for a given spacing, *l*, increasing the aspect ratio, *h*/*d*, will stabilize the Cassie−Baxter regime, as was also illustrated by Yoshimitsu et al.[5] Sample P12 was superwettable when its surface was hydrophilic: this similarity not only shows that roughness with the highest possible aspect ratio, *h*/*d*, will dramatically enhance the wettability of a surface, whether hydrophilic or hydrophobic, but it also entails the ambivalence of topography-enhanced wetting/dewetting, as highlighted already by McHale et al.[21]

Having verified the validity of the Cassie−Baxter model for our submicrometric structures, we investigated Patankar's[12] suggestion that the epicuticular wax crystalloids on the Lotus leaf (200 nm−1 μm) play a significant role in repelling water droplets. We tested this hypothesis by applying the Cassie−Baxter formula for hemispherical tops to our superhydrophobic surfaces (P21, P13, and P12), assuming an ideal contact angle of cuticular wax $\theta_Y = 100°$:[28] the Cassie−Baxter formula predicts apparent contact angles of 150, 155, and 157°, respectively. This result is only indicative because the morphology of the wax crystalloids is very different from those of our model structures. However, we can confirm Patankar's hypothesis that roughness at this scale might stabilize or even be the primary cause of the hydrophobicity of dual-scale topographies. It would be even more interesting for us to compare our results with experimental contact angles of insect wings because our models closely resemble the ordered arrays of nanometric structures shown by Watson et al.[17] Unfortunately, this data is not available at present.

Finally, we verified that the current theoretical predictions for receding angles agree with our experimental values. The experimental receding angles of our Cassie−Baxter drops (P21, P13, and P12) were plotted with eqs 7 and 8 (Figure 6). Our values show a trend similar to the theoretical curves for cylindrical and hemispherical-ended pillars, but more work will have to be done in order to obtain better quantitative predictions.

Conclusions. Regular nanopatterns were fabricated in silicon wafers, and the behavior of water droplets on these surfaces was evaluated before and after chemical hydrophobization. From our results, we conclude that the composite-drop (hemi-wicking) model successfully predicts the advancing angles on hydrophilic patterns. Analogously, the Cassie−Baxter and Wenzel models gave accurate estimates of the advancing angles on hydrophobic patterns. These models are very sensitive to even small variations in the asperity profile, and we show that if the edges of the cylindrical pillars are not sharp, a geometry considering a hemispherical-top rather than a flat one will predict the advancing experimental angles more accurately; we suggest that the same might be true for receding angles. In accordance with Patankar's criterion for designing a superhydrophobic surface, we confirmed that a forest of slender pillars is the most stable water-repellent texture; this same topography exhibited superhydrophilicity, confirming the ambivalence of topography-enhanced wetting/dewetting. Finally, our findings support the suggestion that the epicuticular wax crystalloids of the lotus leaf play a main role in its water-repellent behavior.

Acknowledgment. Many thanks to Adam S. G. Curtis, F. Madani, V. Koutsos, L. Csaderova, N. Blondiaux, M. Robertson, and S. Borzí. The partial support by the EC-funded project NaPa (contract no. NMP4-CT-2003-500120) is gratefully acknowledged. The content of this work is the sole responsibility of the authors.

References

(1) Bico, J.; Thiele, U.; Quere, D. *Colloids Surf., A* **2002**, *206*, 41−46.
(2) Cassie, A. B. D.; Baxter, S. *Trans. Faraday Soc.* **1944**, *40*, 546.
(3) Wenzel, R. N. *Ind. Eng. Chem.* **1936**, *28*, 988−994.
(4) Quere, D.; Lafuma, A.; Bico, J. *Nanotechnology* **2003**, *14*, 1109−1112.
(5) Yoshimitsu, Z.; Nakajima, A.; Watanabe, T.; Hashimoto, K. *Langmuir* **2002**, *18*, 5818−5822.

(6) Shibuichi, S.; Onda, T.; Satoh, N.; Tsujii, K. *J. Phys. Chem.* **1996**, *100*, 19512−19517.
(7) Bico, J.; Marzolin, C.; Quere, D. *Europhys. Lett.* **1999**, *47*, 220−226.
(8) Lau, K. K. S.; Bico, J.; Teo, K. B. K.; Chhowalla, M.; Amaratunga, G. A. J.; Milne, W. I.; McKinley, G. H.; Gleason, K. K. *Nano Lett.* **2003**, *3*, 1701−1705.
(9) Miwa, M.; Nakajima, A.; Fujishima, A.; Hashimoto, K.; Watanabe, T. *Langmuir* **2000**, *16*, 5754−5760.
(10) Oner, D.; McCarthy, T. J. *Langmuir* **2000**, 7777−7782.
(11) Patankar, N. A. *Langmuir* **2003**, *19*, 1249−1253.
(12) Patankar, N. A. *Langmuir* **2004**, *20*, 8209−8213.
(13) Marmur, A. *Langmuir* **2004**, *20*, 3517−3519.
(14) Furstner, R.; Barthlott, W.; Neinhuis, C.; Walzel, P. *Langmuir* **2005**, *21*, 956−961.
(15) Barthloot, W.; Neinhuis, C. *Planta* **1997**, *202*, 1−8.
(16) Shirtcliffe, N. J.; McHale, G.; Newton, M. I.; Perry, C. C. *Langmuir* **2005**, *21*, 937−943.
(17) Watson, G. S.; Watson, J. A. *Appl. Surf. Sci.* **2004**, *235*, 139−144.
(18) Kwok, D. Y.; Lin, R.; Neumann, A. W. *Colloids Surf., A* **1996**, *116*, 63−77.
(19) Roura, P.; Fort, J. *Langmuir* **2002**, *18*, 566−569.
(20) Bico, J.; Tordeux, C.; Quere, D. *Europhys. Lett.* **2001**, *55*, 214−220.
(21) McHale, G.; Shirtcliffe, N. J.; Aqil, S.; Perry, C. C.; Newton, M. I. *Phys. Rev. Lett.* **2004**, *93*, 036102−1.
(22) Abdelsalam, M. E.; Bartlett, P. N.; Kelf, T.; Baumberg, J. *Langmuir* **2005**, *21*, 1753−1757.
(23) Quere, D. *Physica A* **2002**, *313*, 32−46.
(24) Burton, Z.; Bhushan, B. *Nano Lett.* **2005**, *5*, 1607−1613.
(25) Suh, K. Y.; Jon, S. *Langmuir* **2005**, *21*, 6836−6841.
(26) Rozlosnik, N.; Gerstenberg, M. C.; Larsen, N. B. *Langmuir* **2003**, *19*, 1182.
(27) Rasband, W. S. U.S. National Institutes of Health: Betheda, MD, 1997−2005.
(28) Holloway, P. J. *Ann. Appl. Biol.* **1969**, *63*, 145−153.

NL051435T